Survey of Simulation and Diagnostic Techniques for Hypersonic Nonequilibrium Flows

Surendra P. Sharma and Chul Park
NASA Ames Research Center, Moffett Field, California 94035

I. Introduction

WITH the growing interest in transatmospheric vehicles, maneuvering re-entry vehicles, aeroassisted orbital transfer vehicles (AOTVs), and concepts of advanced space transportation systems, greater attention is being given to the aerothermodynamic aspect of hypersonic flows.[1-7] Past research efforts on the subject have been made only to the level required for supporting conservatively designed vehicles such as the Space Shuttle. With the growing need for higher payload and more maneuverable, more efficient vehicles, accurate data on the flowfields and thermal environments around the vehicle are being demanded.

Airflow around hypervelocity vehicles undergoes vibrational excitation, chemical dissociation, and ionization. These chemical and kinetic phenomena absorb energy, change compressibility, cause temperature to fall, and cause density to rise. In high-altitude, low-density environments, the thicknesses of the shock layers can be smaller than the relaxation distances required for the gas to attain chemical and thermodynamic equilibrium. The nonequilibrium phenomena in this environment occur in general to all internal modes (rotation, vibration, and electronic excitation) and external modes (heavy particle translation, electron translation, dissociation, and ionization) of energy.[8-10] These nonequilibrium phenomena affect the design features and operational characteristics of hypersonic vehicles in at least two ways: 1) radiative heating of the vehicles and 2) pressure distribution around the vehicle.

It is known that, behind a strong shock wave in air, the radiative power emitted from the nonequilibrium region close to the shock wave is greater than that from the equilibrium region far from the shock wave.[10-23] Laboratory data from shock tubes[13-17] indicate that the nonequilibrium radiation power may be 2–15 times the equilibrium value.[17] Based on these laboratory data, predictions have been made on the magnitudes of the radiative heating rates over the Apollo and the Fire vehicle (the Fire vehicle was ¼ scale model of the Apollo vehicle). The flight data from these vehicles have shown that the radiative heating rates are substantially smaller than those predicted using the laboratory data. Nevertheless, the radiative heating rate was still of the same order as the convective heating rate for Apollo. For the AOTVs, which are larger than Apollo, the predicted radiative heating rates may be larger than the convective rate.[18] For this reason, accurate determination of the radiative heating rate is deemed necessary for the design of the AOTVs.

Surendra P. Sharma is a research scientist at NASA Ames Research Center in the Aerothermodynamics Branch. He has over 15 years of research experience in the field of physics of fluids. Following research in turbomachines at CSIR, India and IIT, Bombay, India and in physics of MHD lasers at MIT, the author joined the University of Tennessee Space Institute to conduct MHD generators studies. Subsequently, after six years of industrial assignments investigating multi-phase flows and electromagnetics based NDT, he joined NASA Ames in 1986. Presently the author is engaged in theoretical and experimental investigation of the nonequilibrium phenomena associated with real gas effects in hypersonic flows. He received a B.Sc. in Physics, University of Gorakhpur, India, 1960, an M.S. in M.E., PFU, Moscow, USSR, 1968, and a Ph.D. in Physics of Fluids, Massachusetts Institute of Technology, 1978. He is an Associate Fellow of AIAA, member of Sigma XI, and past member of SPE, ASME, and IEEE.

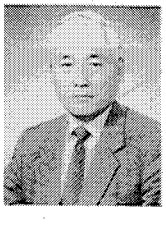

Chul Park is a research scientist at the NASA Ames Research Center in the Aerothermodynamics Branch. He joined Ames Research Center in 1964. His pioneering works include conception and design of aeroassisted aerobrake orbital transfer vehicles (AOTV), study of radiation and radiative transport in air not in thermodynamic equilibrium, environmental impact of Space Shuttle on ozone layer, and impact of meteor penetration in earth's atmosphere. He has authored or coauthored over 90 articles in scientific journals. The author received a B.S. (1957) and an M.S. (1960) in Aeronautical Engineering from Seoul University and a Ph.D. (1964) in Aeronautics (hypersonics) from Imperial College of Science and Technology, London, England. The author is an Associate Fellow of AIAA.

Presented as Paper 87-0406 at the AIAA 25th Aerospace Sciences Meeting, Reno, NV, Jan. 12–15; received Feb. 9, 1988; revision received May 22, 1989.

In the years following the flight tests of Apollo and Fire vehicles, attempts were made to explain the discrepancy between the prediction and the flight data by resorting to two hypotheses: truncation theory and collision-limiting theory. If the shock standoff distance is smaller than the distance required to reach the peak nonequilibrium radiation point, the nonequilibrium radiation does not attain its maximum value; that is, the radiation is truncated.[2,13-17] The Apollo and Fire flight data were obtained in the density regimes lower than those in the shock tubes. At these low densities, there may not be sufficient collisions to maintain the atoms and molecules in their excited states to produce the nonequilibrium radiation. This hypothesis is called collision-limiting theory. Inadequacies of these explanations have been pointed out.[17] A recent work[18] shows that the discrepancy may be due simply to compression of the time scale in the shock layer. A computer program[8,20] has been developed that seemingly reproduces the Fire data. It is necessary at present to further verify the accuracy of such a computer program experimentally.

Modification of pressure distribution around a vehicle is another important effect of nonequilibrium phenomena.[24-26] Because of the finite time required for chemical equilibrium to be reached, the flow in the shock layer over a vehicle behaves nearly as a perfect gas near the nose or leading edge, but as a nearly equilibrium gas toward the trailing edge. Density ratio across a strong shock is approximately 6 for a perfect gas, but increases to as large as 20 in the equilibrium state. The shock-layer thickness is inversely proportional to this density ratio. A thinner shock layer produces a smaller shock angle and consequently a lower postshock pressure. As a result, pressure tends to decrease toward the trailing edge compared with the perfect gas values. In Fig. 1a, the calculated pressure distribution[24] along the surface of a 30-deg half-angle cone at 0-deg angle of attack is shown. The pressure distribution is for a typical Space Shuttle entry flight. As seen here, there is an almost 10% variation between the cone apex and the trailing edge. In Fig. 1b, the corresponding atomic oxygen concentration values are shown. These figures illustrate a connection between pressure and chemical state of the gas in nonequilibrium.

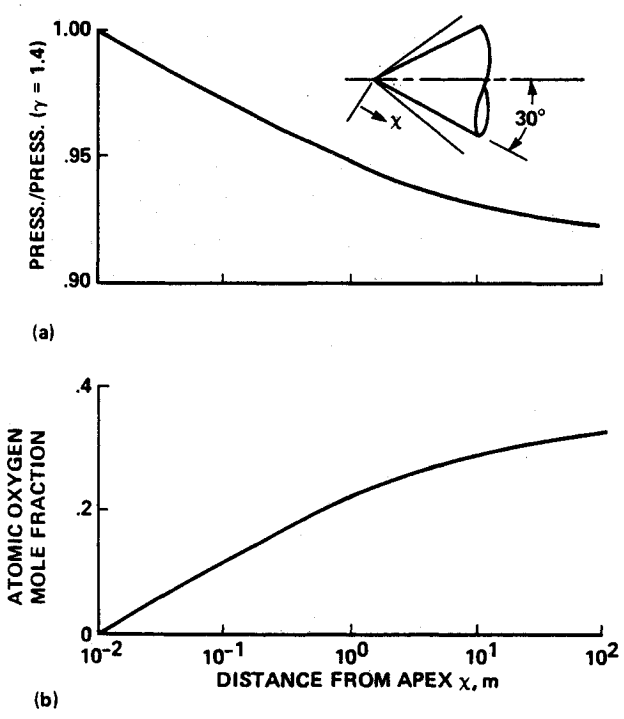

Fig. 1 Nonequilibrium phenomena in an inviscid shock layer over a 30-deg half-angle cone at a flight altitude of 65 km and a flight Mach number of 22, taken from Ref. 20: a) pressures normalized by the perfect gas value; b) mole fractions of atomic oxygen.

As a result of such variation in pressure, the center of pressure moves forward, thereby causing a positive pitching moment. This phenomenon has been observed in the flights of the Space Shuttle.[25] The Space Shuttle was flown with the body flaps deflected 16 deg, instead of the scheduled 7 deg, since the vehicle could not be trimmed to 7 deg. Figure 2a compares the flight-derived pitching moment coefficients with the predicted values. Both the predicted values and flight data are with the body flaps deflected 16 deg. Figure 2b displays the absolute pitching moment coefficients of the vehicle with respect to the center of gravity derived from Fig. 2a.[26] The unexpected large positive pitching moment is believed to have caused the observed nose-up movement of the vehicle.[25] Recently, Park and Yoon,[27] using a two-temperature model, demonstrated that the pitching moments and trim angles of attack are indeed affected by the real gas effects. The computations showed that the extent of the difference in the trim angle of attack between the perfect gas and the reacting gas cases is of the same order as that observed during the Apollo entry flights.[28,29] A similar decrease in pressure due to the real gas effects under laboratory conditions on a cone-hemisphere model has been observed by Nagamatzu et al.[6,7,30] A 50-deg cone-hemisphere was investigated in a 60-cm-diam Mach 10 nozzle over a reflected shock stagnation temperature T_5 of 1000–5800 K. The pressure distribution over the cone-hemisphere decreased at $T_5 = 3000$–5000 K due to real gas effects, compared to the perfect gas values ($T_5 = 1400$ K). Real gas effect on the density flowfields around generic model shapes were studied by some authors[31-34] during the late 1960s and early 1970s. Miller,[31] using the NASA Langley expansion tube, measured shock shapes on basic configurations and compared them with the shock shapes predicted by NASA Ames and

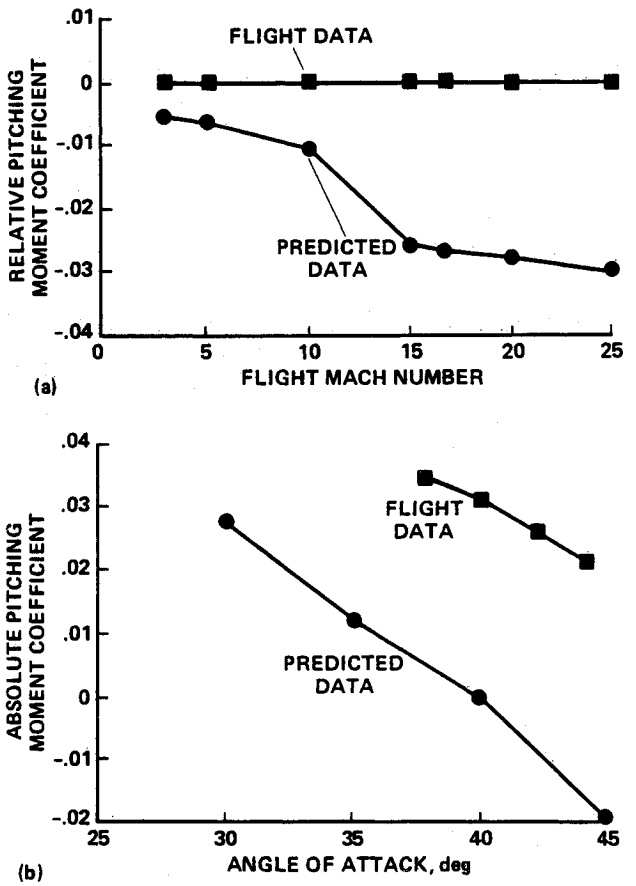

Fig. 2 Pitching moment coefficients on Space Shuttle Orbiter on entry flights: a) flight-derived moments as a function of flight Mach number, taken from Ref. 25; b) absolute moments as a function of angle of attack, taken from Ref. 26.

NASA Langley equilibrium real gas codes. Supported by predictions by Drs. Olstad, Sutton, and Gross at NASA Langley, which accounted for the thermochemical nonequilibrium, the primary cause of the observed discrepancy between the measured and calculated values was attributed to the nonequilibrium within the shock layer. Lobb[32] measured the shock standoff distances over spheres in a ballistic range using schlieren photographs. Spheres of 6.3–12.7 mm diam were launched into a quiescent air at an ambient pressure of 3–20 Torr in these experiments. Spurk[33] conducted similar measurements on a 45-deg half-angle cone in an expansion-type shock tube. Hornung[34] obtained interferograms of the flow over spheres and circular cylinders placed in the test section of a shock tunnel. Recently, Macrossan and Stalker[35] tested a sphere-cone in a flow of nitrogen using a reflection- less shock tunnel. The density, velocity, and temperature in their case were 0.0398 kg/m^3, 6032 m/s, and 2393 K, respectively. The dissociation mass fraction was 0.163, and flow Mach number was 5.7 at the test section. The bow shock profiles taken from interferograms were compared with the predicted values using a one-temperature model. The best agreement between the theory and experiment is estimated to result when a dissociation rate coefficient about 1/15 of the published values is used. The extent of the discrepancy between the measured shock-layer thickness and that predicted by the one-temperature model is nearly identical to that in the experiment by Spurk[33] and Hornung.[34]

The chemical nonequilibrium could conceivably affect other flow phenomena such as separated flows over a deflected flap. This is because the density change accompanying real gas effects could affect the volume of the recirculating region. The characteristics of the separated flow will be those of a perfect as with $\gamma = 1.4$ if the gas is chemically frozen, but will resemble those of a gas with γ less than 1.4 if the gas approaches chemical equilibrium. Onset of separation could be affected by the phenomenon; consequently, the pressure distribution over the deflected flap could be affected.

To determine the effects of chemical nonequilibrium mentioned earlier over a realistic hypersonic vehicle, it would be desirable to conduct an experiment in which all aspects of fluid flow are simulated. Such an experiment is extremely difficult to set up. The only practical alternative is to compute the flow around the vehicle, including the chemical nonequilibrium, and compare the results with the experiments conducted in the facilities under conditions where only certain selected aspects of the flow physics is simulated.

In recent years, new multitemperature models (for example, see Refs. 8, 36, and 37) are beginning to emerge and comparisons with few available[31–35] experimental data on density flowfields are being made for code validation purposes. During this development process research should be concentrated in the several important areas: 1) development of correct models (for example, multitemperature models), better understanding of dissociation-vibrational and rotational relaxation,[38] and inclusion of turbulence and separation phenomena in the fluid physics models; 2) development of better rate coefficient models with more accurate coefficients; and 3) more experimental data for code validation. In this paper we have characterized the role of experimental research, which is required to facilitate the present development process.

The present paper surveys two categories of the problem: 1) how to produce the nonequilibrium flows and how to observe the bulk flow behavior that can be compared with the results of computational fluid dynamics (CFD) computations; and 2) what chemical parameters are needed to be determined experimentally, how the necessary conditions can be produced, and what diagnostic techniques should be used. In the first category of bulk flow behavior observation, the present paper examines shock tubes, shock tunnels and their variations, and ballistic ranges. The types of optical flow visualization techniques required in determining the shapes of the shock waves and their sensitivity requirements and limits are then examined. Laser schlieren and holographic interferometry with a sensitivity several times better than hitherto attained are found to be necessary. Laser-induced fluorescence (LIF) -based planer imaging may play an important role in the bulk flow visualization.

Likewise, in the second category of chemical data acquisition, the present paper examines the operating ranges of the shock tubes to produce the required nonequilibrium conditions. The feasibility of using spectroscopic methods such as emission and absorption spectroscopy, LIF, spontaneous uv laser spectroscopy, and coherent anti-Stokes Raman scattering (CARS) are discussed as diagnostic methods to be used in the measurement of the chemical parameters such as vibrational state distribution, species concentrations, and reaction rate constants.

II. Bulk Flow Behavior Observation

A. What to Measure

1. Radiation

As mentioned in the Introduction, radiative properties of a hot gas are bulk flow quantities measurable directly in the flow. As mentioned therein, radiation data obtained in early years have not yet been fully understood. It would be desirable to repeat the experiments by different, more accurate methods. The limitation with the early shock-tube data on radiation[13–15] was that the data were obtained at many wavelengths using finite-bandwidth monochromators. In any one shot, only three monochromators were operated. Shot-to-shot scatter in radiation intensity existed because of the scatter in the operating conditions of the shock tube. Additional errors were introduced in the process of integrating these intensities over wavelength to obtain the total radiation, because of the compounding of errors in the integration.

For a more accurate determination of radiation intensities, it is desirable to measure two different quantities independently: 1) wavelength- and time-resolved emission spectra and 2) total radiation flux. These measurements could be carried out in two different modes: 1) behind a normal shock in a shock tube without a model and 2) from within a model placed either in a shock tube or in a shock tunnel.

A computer program[10] has been developed with which radiative properties of a gas mixture in nonequilibrium state can be calculated. The program is seen to reproduce the existing shock-tube data[9] to within the accuracy of such experiments. This program should be improved by comparison with more precise experimental data. If such a program can be made accurate, then it could be used for the reverse purpose of diagnosing nonequilibrium flows: From the results of a CFD calculation of a nonequilibrium flow, expected radiation from the flow can be calculated and compared with the results of an experiment conducted to recreate the computed flow conditions.

2. Flowfield Visualization

The illustrations given in Fig. 1 and 2 show that one effective means of testing the accuracy of computation is to compare the thickness of the shock layer or, in general, compare the shock shape with measured data. The simplest demonstration of this can be made with the bow shock standoff distance. It is well known that the shock standoff distance is a sensitive measure of the density ratio across the shock wave.[17,31,32,34,37,39,40] Figure 3 shows the shock standoff distance δ, normalized by the nose radius R, expected in the perfect gas ($\gamma = 1.4$) and in equilibrium gas at hypersonic velocities. The calculated values are compared with the experimental data to show the validity of the theoretical calculation. As seen here, there is nearly a factor of 2.8 difference in shock standoff distance between the frozen (perfect gas) and the equilibrium flows at a Mach number of 20. The difference is greater at higher altitudes because of the greater dissociation at low densities. The difference implies that the shock standoff

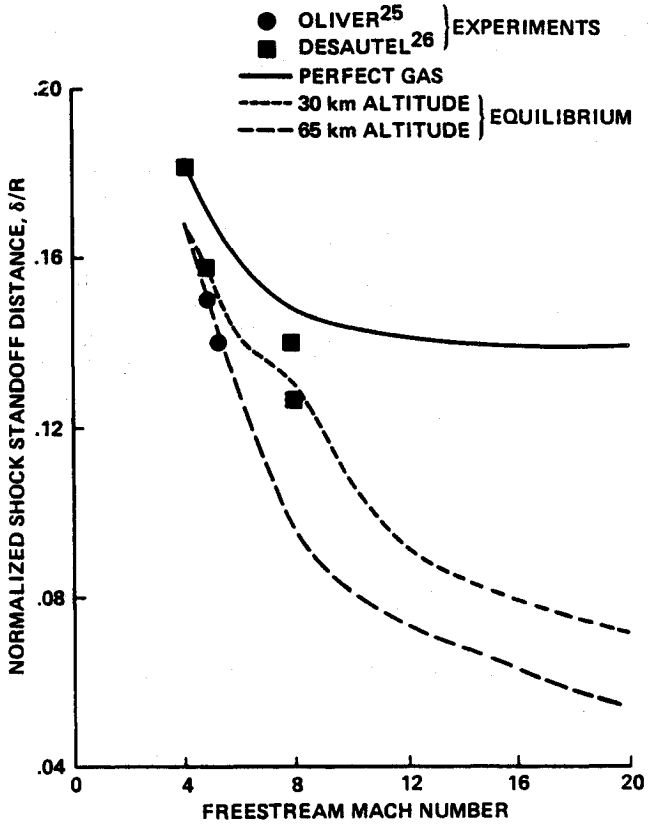

Fig. 3 Bow shock wave standoff distance δ normalized by the nose radius R of a sphere as a function of freestream Mach number for perfect gas and equilibrium gas.

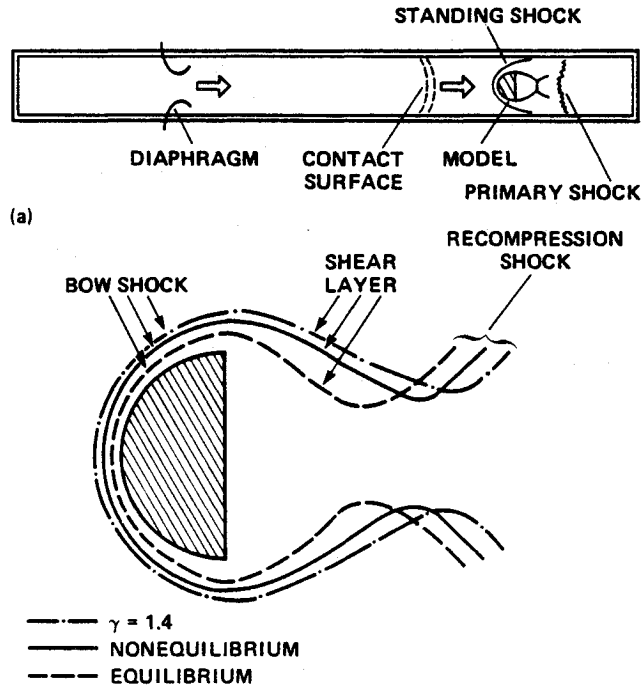

Fig. 4 Schematic showing flow visualization experiment in a shock tube: a) test configuration; b) flowfield around a hemisphere.

distance can effectively provide a test for the accuracy of CFD codes (at least as a necessary condition).

B. How To Produce Test Flows

1. Shock Tubes

There is no known technique for producing a high-enthalpy hypersonic flow with the test gas free of vibrational excitation, dissociation, or ionization in a steady-state condition in a ground-based laboratory. Only the impulse facilities can hope to produce such a flow. There are basically two types of impulse facilities for producing a reacting flow: 1) the shock tube and its variation such as the shock tunnel and 2) the free-flight ballistic range.

In the region behind a primary shock wave in a shock-tube flow, which is known as region 2, the flow Mach number M is 1.87 in the perfect gas with $\gamma = 1.4$ and is slightly higher when real gas effects occur. However, the region 2 flow is already heated by the primary shock. As a result, the enthalpy of the flow reaching the model is high. Up to a primary shock Mach number M_s of 5, there are no real gas effects in region 2. At a M_s of up to 7, one can prevent real gas effects in region 2 by operating at low density, since at low densities the flow residence time is not sufficiently long to cause chemical changes in the gas.

If a blunt body is mounted in the shock tube, as sketched schematically in Fig. 4a, the shock wave over the body will heat the gas again and cause real gas effects to take place. This shock wave is known as a standing shock. At an M_s less than about 7, vibrational excitation and weak dissociation of oxygen is expected behind the standing shock. These phenomena will absorb energy and cause the shock-layer thickness to decrease. As sketched schematically in Fig. 4b, the perfect gas flow should show the largest standoff distance, the equilibrium flow the smallest distance, and the nonequilibrium flow a distance between the two.

The estimated relaxation lengths required for vibrational excitation, oxygen dissociation, and nitrogen dissociation behind a bow shock wave over a blunt body are shown in Fig. 5 at three different initial charging pressure p_1 of the driven section of the shock tube. For a model with a diameter of 5 cm, one expects to see the effects of vibrational relaxation over a distance between about 0.5 and 5 mm, shown by the shaded area in the figure. At a shock velocity of 2.5 km/s ($M_s = 7.3$), which is easily attained using a cold-helium driver, the figure shows that one should be able to measure the effects of vibrational relaxation at a charging pressure of 10 Torr. Dissociation of oxygen should be measurable with p_1 between 1 and 10 Torr, whereas dissociation of nitrogen could be measured at pressures between 0.1 and 1 Torr.

In addition to a sphere model just mentioned, any blunt body, such as a two-dimensional cylinder, large-angle cone or wedge, or even a scale model of a vehicle if the vehicle is sufficiently blunt, can be tested in the shock tube, and the shock shape be measured. In general, the shape of the forebody shock wave will reflect the density change occurring in the shock layer. In the base region of the model, one should be able to measure two other features: the location and angle of the shear layer above the base recirculating region and the recompression shock after the neck region, as sketched in Fig. 4b. These two indicate indirectly the densities in the base recirculating region. Measuring the two parameters will be another means of verifying the accuracy of CFD results. Slender bodies cannot be used for this purpose because there will not be a sufficiently large temperature jump across an oblique shock wave over these bodies at such low Mach numbers to produce significant chemical reactions.

Radiation can be measured in all nonequilibrium environments. The initial charging pressures required to produce sufficiently large nonequilibrium zones can be found in Ref. 11 to be about 10 Torr at a shock velocity below 4 km/s and between 0.3 and 0.1 Torr at 8 km/s or higher.

2. Shock Tunnels

In order to produce a hypersonic flow of high enthalpy, it is necessary to expand the flow from the reflected-shock region, region 5, of a shock tube through a converging-diverging nozzle. Such a facility is known as a shock tunnel (Fig. 6a). Alternatively, one can adiabatically compress the test gas using a piston to produce a similar high-pressure, high-temperature condition. Such a device is known as a gun tunnel. The gas

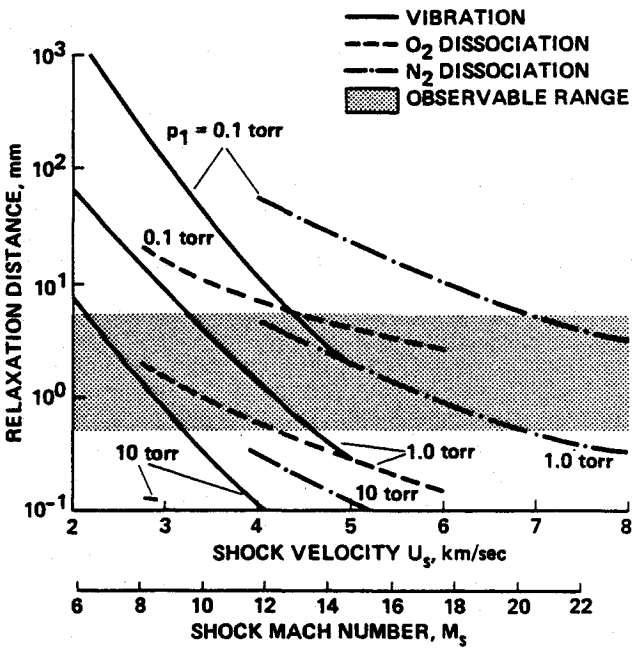

Fig. 5 Estimated relaxation distances for vibrational excitation and oxygen and nitrogen dissociation behind a standing shock in region 2 of a shock tube.

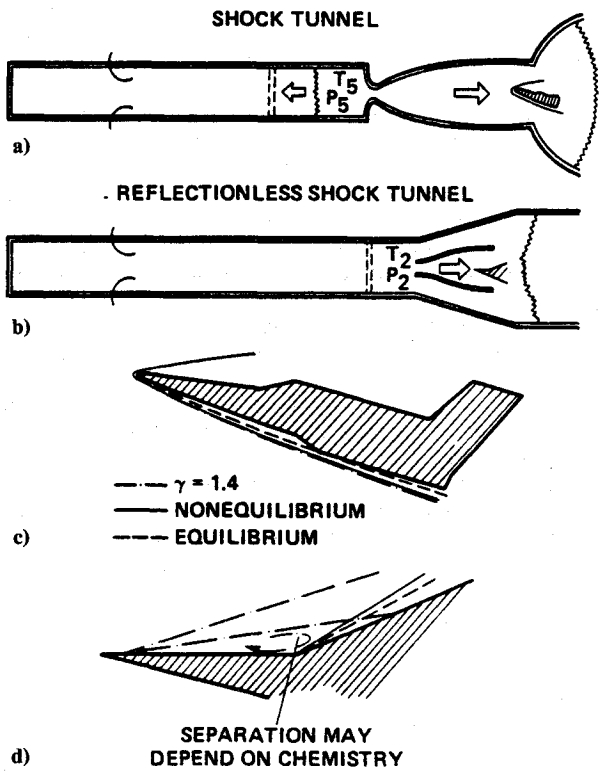

Fig. 6 Schematic showing flow visualization experiments in a shock tunnel and a reflectionless shock tunnel: a) test arrangement for a shock tunnel; b) test arrangement for a reflectionless shock tunnel; c) flowfield around a scale model; d) flowfield over a deflected flap.

flow in the reflected-shock region of a shock tunnel undergoes two shock-compression processes: primary shock and reflected shock. As a result, the enthalpy in the reflected shock is about 2.5 times the static enthalpy behind the primary shock. Because of this, it is relatively easy to produce a high enthalpy.

The same kind of blunt-body model can be tested in a shock tunnel as in a shock tube to observe the effects of chemical nonequilibrium on shock shapes. In addition, the hypersonic nature of the test gas allows meaningful testing of slender bodies such as slender cones, high-lift vehicles, and flap models, as sketched in Figs. 6c and 6d. Unlike that in region 2 of a shock tube, the high Mach number in the test section of a shock tunnel causes a sufficiently large temperature jump across an oblique shock wave over slender bodies, causing significant chemical reactions.

The main drawback of a shock tunnel is the freezing of the chemical reactions in the nozzle, inherent to all facilities with hypersonic nozzle. If the reservoir conditions are at sufficiently high enthalpy, the test gas is dissociated and ionized. As a result, the flow in the test section contains a finite amount of chemical energy in the form of vibration, dissociation, ionization, and electronic excitation. This energy causes the density ratio across a shock wave to be smaller than that in the flight environment: It is closer to the perfect gas value of 6. To minimize this phenomenon, it is desirable to operate the tunnel at high p_5 pressure. If p_5 is high, the vibrational excitation in the test section should be negligible. If the flow enthalpy is such that only oxygen dissociates, the high p_5 will suppress oxygen dissociation in region 5 and also will promote recombination of oxygen atoms in the nozzle. Measurements[41,42] of vibrational relaxation and recombination of N_2 and computations[43] show that one should be able to produce a well-simulated flow up to an enthalpy corresponding to about Mach 15[43] with the stagnation temperature of about 9500 K.

At enthalpies corresponding to Mach numbers higher than 10, dissociation of N_2 produces atomic nitrogen N and nitric oxide NO in the test gas. Production of N can be suppressed by operating the facility at a high pressure, but NO is very stable and cannot be removed. The concentration of NO increases with enthalpy and reaches a value of up to about 5%. The density change across a shock wave suffers slightly from the presence of NO. Nevertheless, if the CFD calculations could theoretically take these effects into consideration, the comparison between the calculated and the measured results will be meaningful.

In a reflectionless shock tunnel, the primary shock wave travels directly through the nozzle and the test section. That is, the flow is expanded from region 2 instead of region 5, as sketched in Fig. 6b. If M_s is less than about 7, region 2 is virtually free of real gas effects. By expanding through a nozzle, therefore, the gas in the test section at the end of the expansion is also free of real gas effects. The total enthalpy in the test flow is the same as that in region 2, which will correspond to a Mach number greater than the shock Mach number, because of the additional kinetic energy in region 2. This method seems to be the most ideal for simulating the flows for flow Mach numbers of up to about 9 or 10.

The reflectionless shock tunnel has its problems. The largest problem is the fact that the available time for expansion is very small: It is equal to the test time available in region 2. The expanding nozzle must be quite small to establish a steady flow within this short available time. And, as a result, the model needs to be very small. To maximize the dimensions of the nozzle and the model, the nozzle must be contoured. Such a nozzle has never been designed or built. Even if such nozzle is built, it will be for only one operating condition.

3. *Ballistic Ranges*

In a ballistic range facility, a model flies through an undisturbed atmosphere. Hence, it is free of the aforementioned problems existing in the shock tubes or shock tunnels. The largest of the existing range facility, such as the one at Arnold Engineering Development Center, Tullahoma, Tennessee, can test models of a diameter up to about 5 cm to a flight velocity of about 6 km/s. For a model of 1 cm diam, a smaller facility at NASA Ames Research Center can produce a flight velocity close to 10 km/s. By matching the Reynolds number of the test model with the prototype flight conditions in such a test, the ratio of the residence time to chemical reaction time, or Damkoehler number, is also matched approximately because

both Reynolds and Damkoehler numbers are proportional to the product of density and length scale. However, the simulation is still imperfect. To produce the same Reynolds and Damkoehler numbers with a small model, pressure must be kept high. At such high pressures, degrees of dissociation and ionization are less than in the low pressures encountered by the full-scale vehicle. The only serious limitation of the ballistic range is that it is difficult to launch an asymmetric model with a large lift-to-drag ratio.

Various flow visualization techniques can be used to photograph the shock patterns around the model. At a model launch velocity of 10 km/s, the bow shock standoff distance on a 20-mm-diam model is typically about 1 mm. The model will travel 0.05 mm within 5 ns, introducing a 5% error in the measurements of shock standoff distance. Hence, the photographic exposure should be kept below about 5 ns.

Figure 7 shows the anticipated range of the ambient pressures required to produce a nonequilibrium reacting flow behind the bow shock over a blunt body. As seen in the figure, the ambient pressure must be maintained at relatively low levels. For example, at the flight velocity of 6 km/s, with a 20-mm-diam model, the gas will attain equilibrium before it reaches the wall if the ambient pressure is about 15 Torr. At ambient pressures below 1.5 Torr, the shock layer is frozen. If the nonequilibrium phenomena at shock velocities above 10 km/s are to be investigated, the ambient pressure must be maintained below 1 Torr.

Table 1 summarizes the foregoing discussions on simulation of nonequilibrium flows in the impulse facilities. As was mentioned, reflectionless shock tunnels offer a nearly perfect simulation at Mach numbers below about 10, whereas ballistic ranges offer a nearly perfect simulation to higher Mach numbers, though only with axisymmetric models. Shock tunnels are the next preferred facilities: They produce correct Mach numbers over the entire Mach number range, but the flows in the test section are partly chemically perturbed. Region 2 of a shock tube can be used for validating CFD calculations, provided the calculations are made for the region 2 conditions.

C. How to Measure

1. *Radiation Detection*

There has been considerable improvement in radiation-sensing technology in the last two decades. The wavelength- and time-resolved spectra can be obtained using gated miniature solid-state sensing arrays. The width of each element is typically 25 μm, and an array of up to 1024 elements is available commercially. Sensitivity of such sensors varies with wavelength, but they can be used for about 250 to about 1100 nm. Gating can be accomplished at arbitrary time point to submicrosecond durations. By placing such a device at the exit focal plane of a spectrograph, one should be able to obtain wavelength- and time-resolved spectra to a wavelength resolution of under 1 nm. The total radiation can be measured directly using pyroelectric detectors that have a nearly flat spectral sensitivity.

Radiation can be measured externally by placing such an instrument outside of the test flow, as was done in Refs. 13–15, or internally from inside a model, as was done in Ref. 16. Such a model can be placed either in a shock tube, to observe the conditions behind the standing shock in region 2 (Fig. 4), or in the test section of a shock tunnel, to observe the shock-layer radiation therein (see Fig. 6).

There is a limitation on the pyroelectric sensors. The signal levels on the sensors are relatively low; thus, the total output (i.e., the intensity integrated over time) must be greater than a certain critical value to provide the required minimum signal-to-noise ratio. In a low-density nonequilibrium flow, the radiation power reaching a sensor becomes typically less than 1 W/cm^2. To satisfy the signal-to-noise ratio requirement, the rate of change of radiation intensity must be such that the sensor can collect radiation at a near-steady level over at least 1 μs.

In a typical nonequilibrium flow, radiation varies considerably within a time shorter than 1 μs. One possible method of overcoming this problem is to measure the radiation intensity falling on the wall of the shock tube at a 45 deg with respect to the axis of the tube facing toward the downstream direction. In this configuration, the sensor spatially integrates the radiation, starting from the shock wave, through the nonequilibrium region first and equilibrium region next, and finally through the boundary layer on the wall. If the shock-tube diameter is larger than the thickness of the relaxation zone, then the integrated value will remain constant over a finite time period. This optical arrangement closely resembles that in the stagnation region of an entry vehicle.

To obtain a sufficient signal-to-noise ratio with a pyroelectric sensor using this optical arrangement, a large-diameter shock tube, on the order of 30 cm or larger, is preferred. Also, to produce a sufficient radiation power, relatively high shock speed, typically greater than 8 km/s, is required. Presently, as far as the authors are aware, the 60-cm electric-arc shock tube (EAST) at Ames Research Center is the only active shock tube that meets these requirements. Work is in progress at Ames Research Center to carry out such an experiment.

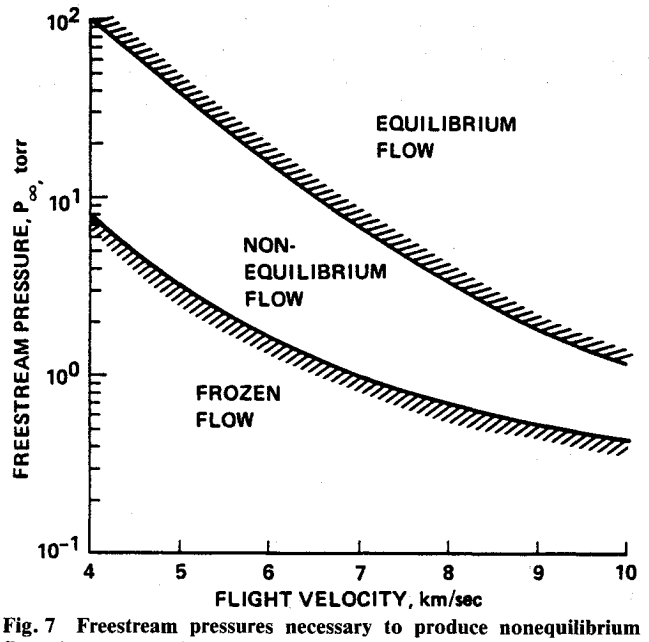

Fig. 7 Freestream pressures necessary to produce nonequilibrium flows in the shock layer over a blunt body of 1-cm nose radius in a ballistic range experiment, as a function of flight Mach number.

2. *Schlieren*

The shape of shock waves around a model can be best determined experimentally using optical flow visualization techniques such as shadowgraph, schlieren, or interferometry. These techniques are well developed.[44–46] Several investiga-

Table 1 Comparison of techniques for measurement of shock shapes

Technique	Typical operating conditions	Test models	Difficulties
Shock tube (Fig. 4)	$0.1 < p_1 < 10$ Torr	Cylinder, sphere, wedge, step	$1.87 < M < 3$
Shock tunnel (Fig. 6)	$6 < M < 25$	Cylinder, sphere, wedge, step, cone, ramp, scale model	Freezing T_v, NO
Reflectionless shock tunnel (Fig. 6)	$M < 10$	Cylinder, sphere, wedge, step, cone, ramp, scale model	Low enthalpy
Ballistic range (Fig. 7)	$1 < p_\infty < 15$ Torr	Sphere, cone	Small model size

tors[30-35,39,40] have successfully used schlieren or infinite fringe interferometer photographs to capture shock shapes around generic model shapes. Excellent to fair resolutions have been obtained at velocities close to 6.0 km/s and at freestream pressures as low as 3 mm Hg ($\rho_\infty = 5.0 \times 10^{-3}$ kg/m^3) in air. As is clear from Fig. 7, if one uses a ballistic range to produce the nonequilibrium test condition, for a 10-mm model flying with a velocity of 6 km/s, the ambient pressure should be kept between 1.75 and 17.5 Torr. Lobb[32] has successfully photographed 12.7-mm sphere models at ambient pressures as low as 5 Torr using a spark light source. In other words, even spark light source based schlieren systems can be effectively used to visualize the nonequilibrium flowfields. With some improvements in the sensitivity, the schlieren methods can cover the entire frozen-to-nonequilibrium-to-equilibrium regimes of hypersonic flows.

The contrast sensitivity of a schlieren system S is given by

$$S = \frac{dC}{d\epsilon} = \frac{2f}{d}$$

where C is the contrast $C = \delta I/I$, I is the light intensity, and ϵ is the angular deflection caused by density gradient, $\epsilon = (L/n_0)(\delta n/\delta s)$ (n is the refractive index, f the focal length of the first field lens, d the size of the light source, s the distance along the light path, and L the width of the wind tunnel). To achieve the same degree of photographic resolution at 1 Torr, which Lobb[32] achieved at an ambient pressure of 5 Torr, one would have to increase the schlieren system's sensitivity approximately by a factor of 5. According to the previous formula, S can be increased by increasing the f. However, so as not to lose light-gathering power, the aperture must be increased proportionately. A large aperture increases cost and chances of misalignment. Therefore, there is a practical limit on the magnitude of f. The only available means of increasing sensitivity beyond what has already been achieved is by reducing the size of the d. This can be achieved by using a laser as the light source.

When the size of the d is reduced, diffraction increases. As a result, additional illumination near the images of boundaries such as wind-tunnel walls and the model being tested fall on the viewing screen, causing distortion in the density field. The use of a graded filter instead of the knife edge is known to improve the sharpness of the schlieren photograph. With a graded filter of a shallow gradient, the field of diffracted light becomes comparatively small and evenly distributed over the viewing screen. If, by these means, the S value is increased, the entire relaxing region in both shock-tube and ballistic range tests would be observable.

3. Holographic Interferometry

Holographic interferometry[47-55] is an interferometric comparison of two object waves separated in time and superimposed in reconstruction. The two waves can be stored on a single hologram (double exposure holographic interferometry), or on two separate plates (dual-plate holographic interferometry). The reconstructed image shows the object with an interference fringe pattern. The fringe pattern represents the difference between the disturbed and undisturbed flow states. The phase difference $\Delta\phi$ responsible for the fringe pattern is given by

$$\Delta\phi \int [n(x,y,z) - n_0]\, ds = N\lambda$$

where s is the length along the light path, N the fringe order number, and λ the wavelength. To determine the flowfield properties, the line integral in this equation must be inverted and solved for $n(x,y,z)$, the refractive index at a specific point in the field. If the refractive index along the width of the test section does not change, then the last equation is simplified to

$$n(x,z) = n_0 + N\lambda/L$$

In Fig. 8, the density difference which a hologram must resolve in the present nonequilibrium application in ballistic ranges is compared with the existing experimental data.[47] As shown, the existing data have resolved densities of 6×10^{-5} g/cm^3, but the present requirement calls for resolving 1.5×10^{-5} g/cm^3. Unlike the case of schlieren, it is not obvious as to how the required fourfold improvement in sensitivity can be achieved. Possibly, since resolution is inversely proportional to the laser wavelength, the desired resolution may be obtained by using a laser light source of shorter wavelength than hitherto used.

4. Laser-Induced Fluorescence-Based Planer Imaging

LIF[56-59] is best viewed as an absorption followed after some finite period of time by spontaneous emission from the excited manifold. The excited manifold may involve the same levels as the incident excitation (resonance fluorescence) or may not (shifted fluorescence). For diagnostic purposes one generally views shifted fluorescence to avoid interferences from spuriously scattered laser light or Mie scattering. In a simplified two-level resonance fluorescence, molecules at level 1 absorb the laser energy and are excited to level 2. The population of the absorbing state and the subsequent fluorescence signal, including the effects of predissociation, absorption, and fluorescence, are described by the following rate equations[56]:

$$\frac{d(N_1/g_1)}{dt} = \frac{(N_2/g_2)}{\tau_2} - W_{12}\left(\frac{N_1}{g_1} - \frac{N_2}{g_2}\right)$$

$$\frac{d(N_2/g_2)}{dt} = -\frac{(N_2/g_2)}{\tau_f} - \frac{(N_2/g_2)}{\tau_D} + W_{12}\left(\frac{N_1}{g_1} - \frac{N_2}{g_2}\right)$$

where $W_{12} = I\sigma_{12}/h\nu$ (I is the laser intensity, σ_{12} the absorption cross section, and $h\nu$ the photon energy); N_1 and N_2 are the population densities of the lower and upper states, respectively; g_1 and g_2 are their degeneracies; τ_2 is the spontaneous radiative lifetime for the transition from the upper state to the lower state; τ_f is the fluorescence lifetime of the upper state including transitions to all accessible levels in the ground electronic state; and τ_D is the predissociation time. For cases where the predissociation rate exceeds all other rates (for example, in the case of O_2 excited by ArF excimer laser, $\tau_D \sim 10^{-11}$ s, whereas τ_{12} and $\tau_f \sim 10^{-5}$ s and $W_{12} \sim 10^7$ s^{-1}), and assuming $N_2 \ll N_1$ and $W_{12} \ll 1/\tau_D$, the population densities can be expressed as

$$N_1 = N_{10} \exp(-W_{12}t)$$

$$N_2 \frac{g_1}{g_2} \simeq \tau_D W_{12} N_{10} \exp(-W_{12}t)$$

The fluorescence signal S_f is defined as the total number of fluorescence photons emitted during a laser pulse duration τ_p and with the laser pulse energy of $E_p = IA\tau_p$, by the excited molecules enclosed in a volume defined by the beam cross section A and the length L of the observed beam. Assuming that the temporal and spacial distributions of the laser beam are uniform, the fluorescence signal can be expressed as

$$S_f = AL\left(\frac{\tau_D}{\tau_f}\right) N_{10}\left(\frac{g_2}{g_1}\right)\left\{1 - \exp\left(-\frac{E_p}{A}\frac{\sigma_{12}}{h\nu}\right)\right\}$$

Note that this expression is a nonlinear function of the laser pulse energy per unit area, E_p/A, which, in turn, determines the extent of the depletion of the ground state population by

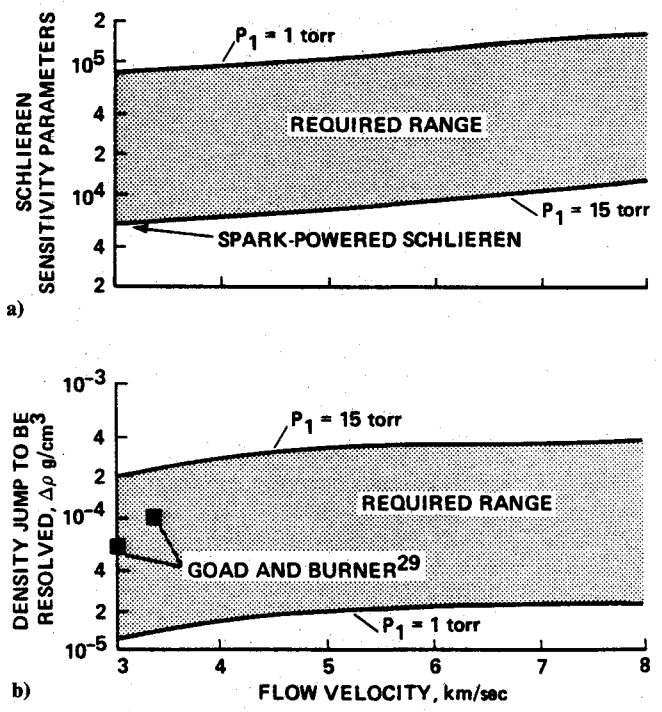

Fig. 8 Sensitivity characteristics required for measurement of the bow shock standoff distance over a blunt body of 1-cm nose radius flown in a ballistic range, compared with the state-of-the-art values for the density jump $\Delta\rho$ to be resolved by holographic interferometry compared with the value attained by Goad and Burner.[47]

the predissociation process. In cases when $W_{12}\tau_p \ll 1$, or when the rate of collisional redistribution is sufficiently high, the depletion of the ground state may be assumed negligible. The fluorescence signal, then, becomes a linear function of the laser intensity

$$S_f = LE_p \frac{\sigma_{12}}{h\nu}\frac{\tau_D}{\tau_f} N_{10}\frac{g_2}{g_1}$$

Since N_{12} is dependent on temperature and density of the gas volume being probed, so is the fluorescence signal.

For LIF imaging the fluorescence signal is typically detected by a vidicon or solid-state array detector. The latter is generally preferable, especially for high-speed acquisition applications. The number of fluorescence photoelectrons detected by such detectors can be estimated as

$$N_{pe} = S_f \eta_c \eta_q T_f$$

where η_c is the optical collection efficiency (for example, $\eta_c = 0.015$ for a $f/2$ collection); η_q the quantum efficiency of the detector (typically ~ 0.15–0.20); and T_f the transmission efficiency of the optical system, which may include special optics such as bandpass filters. If, for example, tests are conducted at the NASA Ames Free Flight Ballistic Range at an ambient pressure of 1 Torr (under these conditions a model of 1 cm diam can achieve velocities up to 10 km/s), with $N_{10} = 3.2\times 10^{16}$ cm^{-3}, $\sigma_{12} \sim 10^{-20}$ cm^2, $\tau_D/\tau_f = 10^{-7}$, and $L = 0.1$ cm, a 500-mJ/pulse ArF excimer laser operating at 248 nm is likely to produce 1.87×10^6 fluorescence photons in oxygen. In this case, using a $f/2$ optical collection system ($\eta_c = 0.015$) with $T_f = 0.9$, a detector with $\eta_q = 0.20$, 5.0×10^3 photoelectrons will be detected, or, in other words, measurement with an uncertainty of 1.4% can be achieved. At NASA Ames Research Center, Laufer and McKenzie[56] have successfully made measurements of temperature and density in room temperature atmospheric oxygen with an uncertainty of less than 1% by using a 15-mJ ArF excimer laser and a $f/6$ collection system.

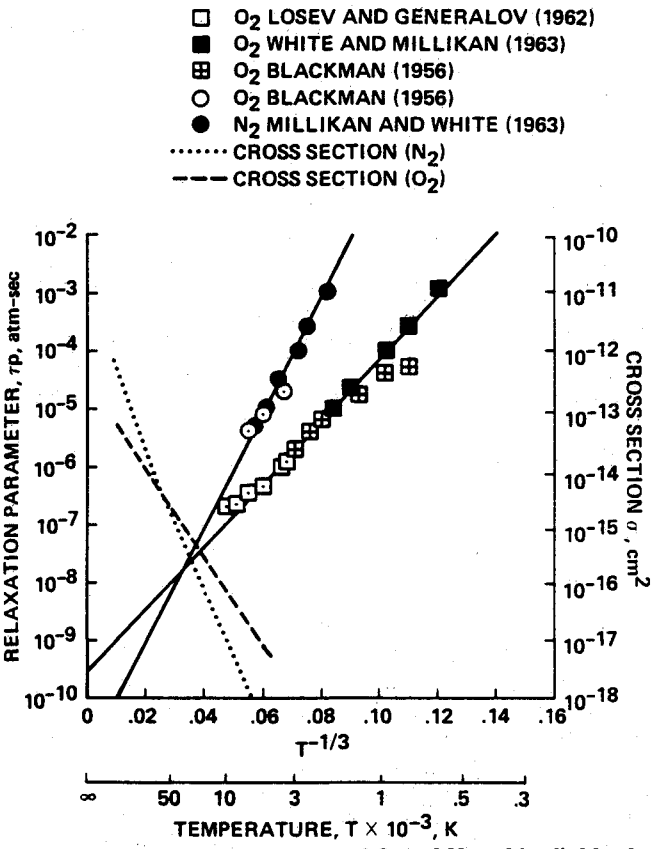

Fig. 9 Vibrational relaxation times of O_2 and N_2 and implied hard-sphere excitation cross sections.

For a planar LIF imaging, a laser beam is used to provide illumination throughout a thin plane using a cylindrical lens. LIF light from the portion of the laser plane illuminating the regions of interest is imaged onto a suitable two-dimensional detector providing an image of the two-dimensional density or temperature flowfield. Unlike the schlieren and holographic processes, LIF planar imaging is free from usual line-of-sight averaging of the flowfield. At low signal levels, the detector is preceded by an image intensifier that can be gated synchronously with the laser pulse to provide instantaneous measurements. The gating time can be as short as 5 ns providing an instantaneous (time integrated over a period of 5 ns) image of the flowfield.

III. Measurement of Chemical Parameters

A. What to Measure

1. Vibrational Excitation

The general problem of the rate processes in nonequilibrium hypersonic flows has been discussed elsewhere in the literature (see, for example, Ref. 2). As the gas temperature is raised, the first nonequilibrium phenomenon to occur is molecular vibration. The vibrational nonequilibrium affects the flow in two ways. First, when vibration is excited, the effective γ approaches 9/7 and the density jump across a strong shock wave becomes 8, a 30% increase from the perfect gas value of 6. This increase in density appreciably alters the flowfield. Second, dissociation reactions are affected because dissociation occurs preferentially from excited vibrational states.

Traditionally, the vibrational relaxation phenomenon has been described using the Landau-Teller formula. The vibrational relaxation time τ that enters into the formula has been measured by many investigators[60–62] and has been collated and expressed using a single formula by Millikan and White.[62] This formula becomes inapplicable at Mach numbers above 10 for the following two reasons:

The first problem is that the relaxation time data are not accurate at high temperatures. In Fig. 9 the vibrational relax-

ation parameters τ_p for N_2 and O_2 are shown with the left-hand-side ordinate. The experimental data are available for temperatures up to about 8000 K. The solid lines are the correlation formulas of Milikan and White for the gases. The formula closely represents the measured data at temperatures below about 5000 K. Between 5000 and 8000 K, the formula tends to underestimate the relaxation times. The dashed lines correspond to the right-hand-side ordinate and are the effective hard-sphere cross sections corresponding to the relaxation times determined using the approximation $1/\tau = \sigma \bar{C} N$, where $\bar{C}$ is the thermal speed of the molecule, and N is the number density of the colliding particles. The cross section σ cannot be larger than the elastic cross section, which is on the order of 3×10^{-16} cm^2. As seen here, the implied cross sections exceed the elastic value. Obviously the correlation formula is invalid at the high temperatures.

The second problem is the change in the nature of relaxation at high temperatures. The Landau-Teller formula correctly describes the excitation of the first ($v = 1$) vibrational state from the ground ($v = 0$) state. As the temperature increases, the kinetic energy of the colliding particles becomes higher than the vibrational energy gap, and, as a result, the collisions not only excite the neighboring energy levels, but also the next higher levels. The process is no longer linear, as implied by the Landau-Teller formula, but resembles a diffusion process (see, e.g., Ref. 52). The phenomenon increases the relaxation time and makes the relaxation rate proportional approximately to an sth power of the temperature difference, where s is greater than unity.[9,63]

In Ref. 9, vibrational temperature of the ground electronic state of N_2 was calculated accounting for the earlier two phenomena for a one-dimensional flow at a shock velocity of 6.4 km/s. The vibrational distribution of the ground electronic state of N_2 is important because it contains the largest amount of vibrational energy in air, affects the dissociation rate of N_2 and production rate of NO, and interacts with electrons. The calculated vibrational temperatures were compared against those determined from the emission spectra of the first negative band of N_2^+ molecules measured in a shock tube.[64] There was a wide discrepancy between the measured and the calculated vibrational temperatures. The measured vibrational temperatures reached equilibrium much more slowly than were calculated, and at the point where radiation intensity reached its peak, the measured T_v was only about half of that calculated. This discrepancy was attributed in Ref. 9 to the deviation of the vibrational temperature of the excited state of N_2^+ from that of the ground state of N_2. To verify the accuracy of this explanation, measurement of the vibrational state distribution of the ground electronic state of N_2 was deemed necessary in the relaxing region.

It is worth noting here that Ref. 9 also compared the calculated rotational temperatures with those determined experimentally in the same experiment.[64] The calculation was based on the assumption that rotational temperature is the same as the translational temperature of the heavy particles. Experimentally, rotational temperature was determined from the emission spectra of the first negative band of N_2^+. The theory and the experiment agreed roughly, but the degree of the agreement is less than desirable. A more refined, precise measurement of rotational temperature would be desirable.

2. Dissociation Rates

There have been numerous experimental measurements of dissociation rates over the years. Several reviews have also been written on the subject. Most exciting experimental data are for temperatures below about 10,000 K. The data have been fitted with a rate coefficient expression of the form

$$K = CT^n \exp\left(-\frac{T_d}{T}\right)$$

where T_d is the characteristic temperature of dissociation, and the exponent n must be chosen to best fit the measured data over the temperature range of interest. Since the measurements were made at below about 10,000 K, n had been selected to best fit the data below 10,000 K. When such an expression is extrapolated to higher temperatures, it tends to predict unrealistically high reaction rates. Thus, determining the rate coefficients at high temperatures remains to be done.

Additionally, as mentioned earlier, the influence of the vibrational nonequilibrium on reaction rates is virtually unknown. In Ref. 9, the best agreement between the computed and measured radiation characteristics was found when the rate coefficients were assumed to depend on a geometrically averaged temperature

$$T_{av} = \sqrt{TT_v}$$

This point needs further experimental verification.

3. Ionization Rates

At conditions typical to an AOTV, the degree of ionization may reach up to about 10%. Ionization affects radiative heating characteristics and interferes with radio transmission. Also, the energy absorbed in ionization is considerable. The ionization occurs in air through associative ionization, charge transfer, and electron impact ionization. The data on associative ionization presently in use had been measured in a shock tunnel (see, for example, Ref. 65). A recent theoretical calculation[66] yields rates that are smaller in magnitude than the measured rates. Virtually nothing is known of the rates of charge transfer at high temperatures. There is only one set of experimental measurement of the electron-impact ionization rates,[67] which shows a fairly large scatter within the data.

In early years, a flight experiment, RAM-C, has been conducted to test whether the ionization phenomena in the shock layer can be correctly calculated (see, for example, Ref. 68). Very few investigators[69,70] were able to model the experimental data, and even their model is far from complete. This affair can be attributed to a great extent to the uncertainties in the rate data.

B. How to Produce Test Flows

The conventional shock tube consisting of one driver chamber and one driven section is an excellent tool for studying the chemical parameters. Driving with cold helium, a shock speed of up to about 2 km/s is obtainable. A cold hydrogen driver enables a shock speed of close to 3 km/s. A combustion driver with a hydrogen-oxygen-helium mixture attains 6 km/s in air, whereas with an electric-arc driver speeds up to about 13 km/s are attainable. A piston-compressed helium or hydrogen driver can produce shock strengths that are higher than achieved by combustion and slightly weaker than those of electric-arc drivers. Even higher shock speeds can be achieved with an explosion driver. Nagamatzu[71,72] was able to produce 16.5 km/s with the combustion of a stoichiometric mixture of H_2 and O_2 in 75% helium in the driver. In MHD experiments,[72] with transverse magnetic fields across a 10-cm-diam tube, Mach 30 was achieved with the gas temperature of 10,000 K. Compton and Cooper[73] produced shock velocities of 67 km/s using an explosive driver at NASA Ames Research Center.

Shock tubes are unique in creating a homogeneous sample of gas, heated to an enthalpy and pressure calculable and selectable from the state of the undisturbed gas and the measured shock velocity. The homogeneity of the test gas slug produced is limited by the growth of wall boundary layer and the mixing of the driver with the driven gas in the contact-surface region. Test gas slug length extending one tube diameter or more is required to produce a planar shock normal to the wall. At the low densities of present concern, the mixing in the contact-surface region can be very extensive.

The operating conditions of the shock tubes appropriate for the purpose of studying the nonequilibrium relaxation phe-

nomena behind the primary shock can be deduced from the relaxation lengths of the reactions to be observed, shown in Fig. 10. According to the figure, vibrational relaxation at shock velocities under 3 km/s can be studied at a charging pressure p_1 of 3–10 Torr, whereas dissociation of oxygen and nitrogen requires 0.3–3 Torr and 0.1–1 Torr, respectively.

C. How to Measure

1. Absorption and Emission Spectroscopy

In Ref. 64, emission spectra were measured to determine rotational and vibrational temperatures of an excited state of N_2^+. Such emission measurements can be easily made at any low pressures, provided such test flow can be produced free of contamination. As mentioned earlier, however, such measurement does not yield information on vibrational distribution of the ground electronic state needed in the study of nonequilibrium flow phenomena.

Using an absorption technique, the vibrational distribution of the ground electronic state of a molecule can be determined, as well as concentrations of the species. An absorption measurement can be made either using a narrow, single wavelength or a broadband continuum source. A continuum source must have an effective blackbody temperature substantially greater than that of the gas under study. Spark sources of over 40,000 K temperature are available commercially. Excimer lasers can be used as a continuum source to a wavelength as short as about 1900 Å. A single wavelength light source can be obtained using a tunable laser. However, the absorption characteristics in this case depends critically on the widths, shifts, and shapes of the absorbing line. Such line shape parameters are not well known in the environments of interest.

Broadband absorption, in which absorption occurs by a cluster of lines, eliminates the need for individual line shape information, provided the experiment is conducted in a weakly absorbing (nearly optically thin) regime. Figure 11 shows the absorption of a wideband light source by the $\alpha^1\Pi_g - X^1\Sigma_g^+$, $b'^1\Sigma_u^+ - X^1\Sigma_g^+$, and $b^1\Pi_u - X^1\Sigma_g^+$ absorption bands[74–79] of nitrogen molecules. All three transitions have the ground state as the lower state. The calculations were performed for an equilibrium flow at a charging pressure of $p_1 = 1$ Torr, shock velocity of 6 km/s, region 2 pressure of $p_2 = 0.5$ atm, and translational and vibrational temperatures of 8810 K, the number density of N_2 of 2.7×10^{17} cm^{-3}, electron density of 2.4×10^{14} cm^{-3}, and colliding particle number density of 6×10^{17} cm^{-3}, using the electronic transition moment values given in Ref. 78 with a program developed at Ames Research Center.[80]

For a reliable absorption measurement, absorption of 10–20% is required. As Fig. 11 shows, absorption is negligible at wavelengths higher than 1800 Å, is about 7% at 1700 Å, and about 40% at 1600 Å. These absorption values are subject to uncertainties in the electronic transition moments and thus may vary as more accurate values are used. However, it is evident that the absorption technique for measurements in nitrogen will be useful only in the vacuum uv region of the spectrum. Similarly, the Schumann-Runge, $B^3\Sigma_u^- - X^3\Sigma_g^-$ transition, of oxygen molecule, which has a strong absorption band in the vacuum uv below 1900 Å, can be used for the measurement of vibrational temperature and species concentration of oxygen molecules. The β and γ transitions of NO in the range of 2000–3600 Å are also promising candidates for measurements using the absorption technique. Absorption measurements in these wavelength ranges have been conducted with relative ease in a shock tube using a spark light source and sapphire windows.[81] For O_2 and NO, excimer lasers can be used as the light source.

2. Fluorescence

Fluorescence spectroscopy involves the selective excitation of the species under investigation and the detection of the resulting fluorescence signal normal to the incident beam. Since the basic pumping mechanism involved is light absorption, the fluorescence technique also measures the ground state temperatures. However, in the fluorescence techniques, only a very small fraction of incident light needs to be absorbed in order to produce a reasonable signal-to-noise ratio, compared to 10–20% of absorption required in the absorption method. As a result, the technique can be used at densities lower than those required for absorption measurement. The bands usable for absorption measurement are all usable for fluorescence.

Since the upper states of the absorption bands involved have no other emission path than those being used for excitation, the same band system must be used for both excitation and fluorescence. Thus, the fluorescence measurement must be made at wavelengths only slightly different from those of excitation. However, the signal wavelength being so close to the

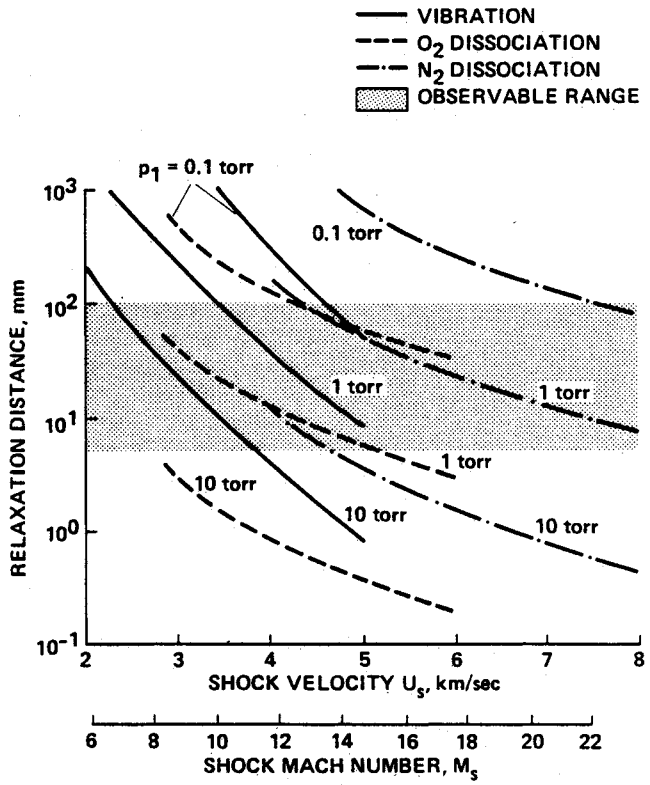

Fig. 10 Estimated relaxation distances for vibrational excitation and oxygen and nitrogen dissociation behind a primary shock, region 2, in a shock tube.

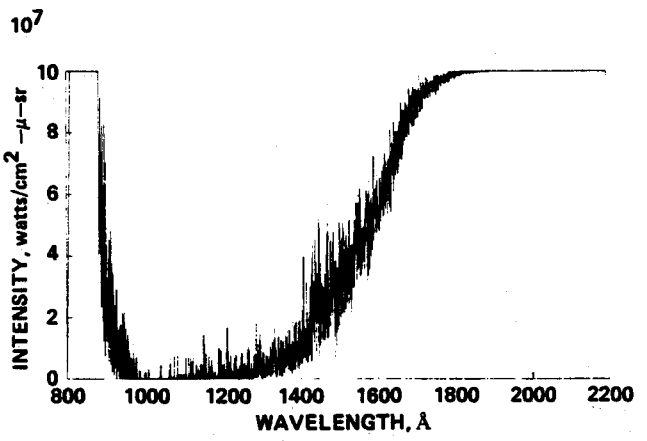

Fig. 11 Calculated absorption spectra of N_2 at N_2 number density of 2.7×10^{17} cm^{-3}, electron density of 2.4×10^{14} cm^{-3}, total colliding particle number density of 6×10^{17} cm^{-3}, and temperature (translational, vibrational, and rotational) of 8810 K, calculated using the electronic transition moments in Ref. 78.

excitation wavelength, stray light might get into the spectrographic instrument. The exciting incident light beam is scattered by the target gas, and a portion of the scattered light enters the spectrograph. Since the fluorescence wavelength is only slightly different from that of excitation, it would be virtually impossible to eliminate the unwanted light using a filter, and hence both the excitation radiation and fluorescence radiation enter the instrument and are diffracted by the grating in the spectrograph. The spectrograph would understandably be operated in such a way that the diffracted excitation signal would fall on the inner walls of the spectrograph, rather than entering the sensing element at the exit focal plane. However, since the walls of the spectrograph are not totally black, the excitation signals reflected from the walls will reach the sensing element as a stray light. Ingenious means must be devised to reduce the stray light.

As discussed in Sec. II, LIF can be used to detect species concentrations with uncertainties around 1.4% under hypersonic conditions. However, while making quantitative assessments from an LIF experiment, one must consider effects of collisional quenching of the fluorescence phenomena. In cases where the quenching energy transfer dominates, the laser pulse duration must be

$$\tau_p \ll \tau_q$$

for the linear approximation to be valid, where τ_q is the characteristic quenching time. Another way to account for quenching is not to avoid its influence, but to experimentally measure the quenching decay rate and include it in the rate equations. For the detection of most atoms (for example, N, O, H) and some molecules which possess absorption bands below 200 nm, "multiphoton" LIF processes can be used. Such multiphoton techniques not only allow access to vacuum uv transitions using uv lasers, but also have another advantage; namely, the spectral region of the fluorescence signal is well removed from the incident laser excitation and is thus well separated from the interfences from single-photon excited fluorescences, rotational Raman scattering, and elastically scattered laser light. A two-photon excitation rate per molecule can be expressed as[82]

$$W_{12} = I\frac{\{\alpha_{12} I\}}{h\nu}$$

where α_{12} is the two-photon absorption cross section. For most atomic species (H, C, N, and O), α_{12} is on the order of $\sim 10^{-27}$ cm^4/W. For a typical laser intensity ($I \sim 10^8$ W/cm^2), $I\alpha_{12} = 10^{-19}$ cm^2, meaning that the effective absorption for a two-photon transition can be comparable to a single-photon absorption when a tightly focused high power uv laser is used, and a two-photon LIF can provide similar accuracies in the measurements.

3. *Spontaneous Raman Spectroscopy*

Spontaneous vibrational Raman scattering[59,82,83] is one of the many scattering processes that can be used for local measurement of temperature and species concentration. Although spontaneous Raman scattering is weak compared to other light scattering processes such as CARS and LIF, it has the advantages of 1) gas species selectivity, 2) simple interpretation of the signal (no collisional quenching), and 3) simultaneous multiproperty determination (major species concentration, temperature, and pressure). In vibrational Raman scattering, the scattered light is either red-shifted (Stokes) or blue-shifted (anti-Stokes) when an upward ($\Delta v = +1$) or downward ($\Delta v = -1$) jump in the vibrational level is made. With the advent of uv excimer lasers, dramatic improvements in the single-pulse vibrational Raman scattering are made. The excimer-based probe can provide excellent spatial (0.1×0.1 mm^2) and time (25 ns) resolution. These improvements result from the lower divergence of the uv excimer and the increased Raman cross section ($\propto \nu^4$; 15–20 times higher) at uv wavelengths.

The number of detected Stokes photons E_s can be estimated by the following expression:

$$E_s = \frac{Q_s C_s \Omega L N \sigma_s E}{h\nu_s}$$

where Q_s is the detector quantum efficiency; C_s the optical efficiency at Stokes frequency υ_s; E the laser energy (Joules); N the number density of molecules (cm^{-3}); σ_s the Raman cross section at ν_s (m^2/sr); Ω the solid angle of the optics (sr); and L the detected length of the laser beam. In a typical shock-tube experiment in nitrogen with a charging pressure $p_1 = 1$ Torr, shock velocity of 6 km/s, region 2 pressure of $p_2 = 0.5$ atm, translational temperature T_2 of 8100 K, and number density N_2 of 2.7×10^{17} cm^3, a 600-mJ KrF excimer operating at 248 nm will produce 5×10^5 detected Stokes photons scattered by the ground state molecules. Here we have assumed that $C_s = 0.06$, $Q_s = 0.20$, $\Omega = 0.35$ sr (ℓ1.5), $\nu_s = 6.993 \times 10^{13}$ Hz, $E = 600$ mJ, $N = 2.77 \times 10^{17}$ cm^{-3}, and $\sigma_{s_{N_2}} = 1.2 \times 10^{-33}$ m^2/sr and that about 30% of the molecules are in the ground state. It is further assumed that the detection is done in a forward-scattering mode providing an active length of the laster beam $L = 10$ cm. At an elevated temperature of 8810 K, the signal would be spread over a bandwidth of 352 cm^{-1} among 72 rotational lines from $J = 0$ to 142 (only even J values). The peak will occur at $J = 38$ separated by about three wave numbers from the $J = 36$ and $J = 40$ lines. Since about 7.5% of ground state molecules will be in the $J = 38$ state, the peak will produce 3.7×10^4 detected Stokes photons, with a S/N of about 200 and an accuracy of 0.5%. The signals from higher vibrational levels will be weaker. For example, assuming an equilibrium vibrational population at $T_v = 9000$ K, signals with a 10% accuracy from vibrational levels up to $v = 14$ can be easily recorded. The signal levels can be further improved by increasing the efficiency of the optical collection system and using multipass systems.[59,82]

4. *Coherent Anti-Stokes Raman Spectroscopy*

In the CARS technique,[84–92] two high-powered laser beams at angular frequencies ω_1 and ω_2 are focused together in a sample. As a result of mixing, a coherent beam resembling a low-intensity laser beam at frequency $\omega = \omega_1 + (\omega_1 - \omega_2)$ is generated in the medium. Typically ω_2 is varied to obtain a Raman spectrum. The power generated in the CARS conversion is expressed as[84]

$$P = \left(\frac{\pi}{\lambda}\right)^2 \left(\frac{12\pi^2\omega}{c^2}\right)^2 |\chi^{(3)}|^2 P_1^2 P_2$$

where $\chi^{(3)}$ is the third-order susceptibility, λ is the average wavelength involved, and P_1 and P_2 are the powers of the pump laser and the laser at the Stokes frequency, respectively. The CARS power becomes larger when there is a resonance such as vibrational or rotational excitation. The susceptibility is a sum of resonant and nonresonant parts in the form

$$\chi^{(3)} \equiv \chi_{\text{res}} = \chi'_{\text{res}} + i\chi''_{\text{res}} + \chi^{NR}$$

where, for simplicity, the subscript 3 has been dropped and the superscript NR designates nonresonance. It is the presence of this nonresonant susceptibility that limits the sensitivity of the technique, because one can record Raman spectra only to the extent that χ'_{res} exceeds χ^{NR}; that is,

$$\frac{\text{signal}}{\text{noise}} = \frac{1}{\epsilon}\left(\frac{\chi'_{\text{res}}}{\chi^{NR}}\right)$$

where ϵ denotes the fractional mean square deviation of the pump laser power.

Table 2 Raman cross sections for diatomic molecules

Molecule	Raman shift, cm^{-1}	$\chi^{NR}/(\chi^{NR})_{N_2}$ [a]	$\frac{d\sigma}{d\Omega}\Big/\left(\frac{d\sigma}{d\Omega}\right)_{N_2}$ [b]
H_2	2331	1.00	1.00
O_2	1556	0.96	1.20
NO	1877	3.10	0.55
H_2	4155	—	2.20

[a] $(\chi^{NR})_{N_2} = 1.35 \times 10^{-18}$ cm³/erg ($T = 300$ K, 1 atm).
[b] $(d\sigma/d\Omega)_{N_2} = 4.4 \times 10^{-31}$ cm²/sr.

Table 3 Comparison of spectroscopic techniques for measurement of chemical parameters in shock tubes

Technique	Driven-section pressure	Parameters measured	Difficulties
Emission	$p_1 > 0.05$ Torr	T_{rot}, T_v of excited states	Ground state inaccessible
Absorption	$p_1 > 1$ Torr	T_v of ground states, N_2, O_2, NO, N, O conc.	Linewidth uncertain if single line
LIF	$p_1 > 0.1$ Torr	T_v of ground states, N_2, O_2, NO, N, O conc.	Quenching a problem
Spontaneous	$p_1 > 1$ Torr	T_{rot}, T_v, N_2, O_2, NO conc.	Low signal level
CARS	$p_1 > 1$ Torr	T_{rot}, T_v, N_2, O_2, NO conc.	Expensive instrumentation

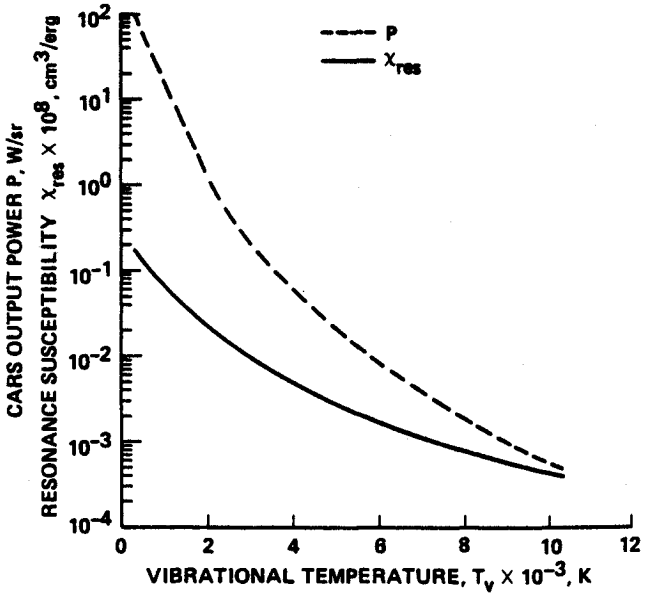

Fig. 12 Calculated resonant susceptibility and output power in the CARS experiment conducted with N_2 at a pressure of 0.5 atm with laser powers P_1 and P_2 of 5 and 0.5 MW, respectively.

In Table 2, experimentally determined values of χ^{NR} are listed for the gases of present interest. Let us examine the sensitivity parameter of a typical CARS system: $P_1 = 5$ MW at 532 nm, pulsed (20 ns) of a frequency-doubled, Neodymium YAG laser with 0.03 cm^{-1} linewidth, and $P_2 = 0.5$ MW, a dye laser. For the 300–12,000 K range, assuming a constant pressure of 0.5 atm, the resonance susceptibility and CARS signal power are calculated and shown in Fig. 12. It can be seen from the figure that the CARS power decreases by five orders of magnitude as the temperature is increased from 300 K to 8810 K. This dramatic drop in the signal is due to the decrease in the number density ($\propto N^2$), the small relative difference between the lower state and upper state populations, and the increase in the linewidth. Even at this reduced level, CARS signals of the order of a milliwatt are predicted, which are sufficiently large to be detected.

Table 3 summarizes the foregoing discussions on the techniques of determining chemical parameters in a nonequilibrium flow. As just stated and in the table, absorption, fluorescence, and CARS all seem to be useful for this purpose.

IV. Concluding Remarks

For the purpose of validating CFD calculations including nonequilibrium chemical reactions, comparison with the experimental data on radiation intensity and schlieren or holographic interferogram seem most appropriate, because of the strong influence of nonequilibrium phenomena on radiation and shock shapes. Various shock tubes, shock tunnels, and ballistic ranges can be used for producing required nonequilibrium conditions by charging the devices with initial pressures in the range of 0.1–15 Torr depending on the reactions to be studied. Almost exact simulation is possible using a reflectionless shock tube in the relatively low-Mach-number range, or using a ballistic range over most of the interested Mach number range. Shock tubes and shock tunnels can be used for the same purpose if the CFD calculation is carried out for the experimental conditions. Because of the relatively low pressures, sensitivity requirements on the flow visualization techniques are stringent. A schlieren system using a laser source and a graded filter should improve the sensitivity by a factor of 5 over that of a conventional spark-powered system and meet the requirement. Holographic interferometry can be useful if its sensitivity can be increased by a factor of about 4. LIF planar imaging, which can provide measurement accuracies higher than 98.6% under simulated hypersonic conditions, may be an excellent tool for flow visualization.

Experimental data relating to the chemical state of the gas crucial to high-Mach-number regimes are mostly unknown and need to be obtained experimentally. For the determination of such chemical parameters, shock tubes of various sizes and strengths are needed. Laser absorption, LIF, and spontaneous Raman spectroscopy look promising in determining vibrational state distributions, species concentrations, and chemical rate parameters.

References

[1]Howe, J. T., "Introductory Aerothermodynamics of Advanced Space Transportation Systems," *Journal of Spacecraft and Rockets,* Vol. 22, No. 1, Jan.–Feb. 1985, pp. 19–26.

[2]Park, C., "Problems of Rate Chemistry in the Flight Regimes of Aeroassisted Orbital Transfer Vehicles," *Progress in Astronautics and Aeronautics: Thermal Design of Aeroassisted Orbital Transfer Vehicles,* Vol. 96, edited by H. F. Nelson, AIAA, New York, 1985, pp. 511–537.

[3]Holden, M. S. "A Review of Aerothermal Problems Associated with Hypersonic Flight," AIAA Paper 86-0267, Jan. 1986.

[4]Jaffe, R. L., "Rate Constants for Chemical Reactions in High-Temperature Nonequilibrium Air," *Progress in Astronautics and Aeronautics: Thermophysical Aspects of Re-entry Flows,* Vol. 103, edited by J. N. Moss and C. D. Scott, AIAA, New York, 1985, pp. 123–151.

[5]Stollery, J. L., "Hypersonic Flow Problems Associated with Future Space Vehicles," Cranfield Institute of Technology, Cranfield, UK, Rept. 8512, 1985.

[6]Nagamatzu, H. T., Geiger, R. E., and Shear, R. E., Jr., "Real Gas Effects in Flow Over Blunt Bodies at Hypersonic Speeds," *Journal of Aerospace Sciences,* Vol. 27, No. 4, April 1960, pp. 241–251.

[7]Nagamatzu, H. T. and Geiger, R. E., Jr., "Hypersonic Gas Dynamics," AIAA Paper 85-0999, Jan. 1985.

[8]Park, C., "Convergence of Computation of Chemically Reacting Flows," *Progress in Astronautics and Aeronautics: Thermophysical Aspects of Re-entry Flows,* Vol. 103, edited by J. N. Moss and C. D. Scott, AIAA, New York, 1986, pp. 478–513.

[9]Park, C., "Assessment of Two-Temperature Kinetic Model for Dissociating and Weakly-Ionizing Nitrogen," AIAA Paper 86-1347, June 1986.

[10]Park, C., "Calculation of Nonequilibrium Radiation in the Flight Regimes of Aeroassisted Orbital Transfer Vehicles," *Progress in Astronautics and Aeronautics: Thermal Design of Aeroassisted Orbital Transfer Vehicles,* Vol. 96, edited by H. F. Nelson, AIAA, New York, 1985, pp. 395–418.

[11]Arnold, J. O. and Whiting, E. E., "Nonequilibrium Effects on Shock-Layer Radiometry during Earth Entry,"*Journal of Quantitative Spectroscopy and Radiative Transfer,* Vol. 13, No. 9, 1973, pp. 861–870.

[12]Cooper, D. M., Jaffe, R. L., and Arnold, J. O., "Computational Chemistry and Aeroassisted Orbital Transfer Vehicles," *Journal of Spacecraft and Rockets,* Vol. 22, No. 1, Jan.–Feb. 1985, pp. 60–67.

[13]Allen, R. A., Rose, P. H., and Camm, J. C., "Nonequilibrium and Equilibrium Radiation at Super-Satellite Re-entry Velocities,"AVCO Everett Research Lab., Everett, MA, Research Rept. 156, Sept. 1962.

[14]Teare, J. D., Georgiev, S., and Allen, R. A., "Radiation from the Nonequilibrium Shock Front," AVCO Everett Research Lab., Everett, MA, Research Rept. 112, Oct. 1961.

[15]Camm, J. C., Kivel, R. L., Taylor, R. L., and Teare, J. D., "Absolute Intensity of Nonequilibrium Radiation in Air and Stagnation Heating at High Altitudes," AVCO Everett Research Lab., Everett, MA, Research Rept. 93, Dec. 1959.

[16]Shirai, H. and Park, C., "Experimental Studies of Radiative Base Heating of a Jovian Entry Model," *Progress in Astronautics and Aeronautics: Entry Heating and Thermal Protection,* Vol. 69, edited by W. B. Olstad, AIAA, New York, 1980, pp. 148–171.

[17]Park, C., "Calculation of Radiation from Argon Shock Layers," *Journal of Quantitative Spectroscopy and Radiative Transfer,* Vol. 28, No. 1, Jan. 1982, pp. 29–40.

[18]Davies, C. B. and Park, C., "Aerodynamic and Thermal Characteristics of Modified Raked-Off Blunted Cone," AIAA Paper 86-1309, June 1986.

[19]Seiff, A., Reese, D. E., Sommer, S. C., Kirk, D. B., Whiting, E. E., and Niemann, H. B., "PAET, An Entry Probe Experiment in the Earth's Atmosphere," ICARUS: International Journal of Solar System Studies, Vol. 18, No. 4, 1973, pp. 525–563.

[20]Cauchon, D. L., "Project Fire Flight 1 Radiative Heating Experiment," NASA TM X-1222, April 1966.

[21]Cauchon, D. L., "Radiative Heating Results from the Fire 2 Flight Experiment at a Reentry Velocity of 11.4 Kilometers per Seconds" NASA TM X-1402, July 1967.

[22]Lee, D. B. and Goodrich, W. W., "The Aerothermodynamic Environment of the Apollo Command Module during Super-Orbital Entry," NASA TN D-6792, April 1972.

[23]Park, C., "Radiation Enhancement by Nonequilibrium in Earth's Atmosphere," *Journal of Spacecraft and Rockets,* Vol. 22, No. 1, Jan.–Feb. 1985, pp. 27–36.

[24]Rakich, J. V., Bailey, H. E., and Park, C., "Computation of Nonequilibrium, Supersonic Three-Dimensional Inviscid Flow Over Blunt-Nosed Bodies," *AIAA Journal,* Vol. 21, No. 6, June 1983, pp. 834–841.

[25] Compton, H. R., Scallion, W. J., Suit, W. T., and Schiess, J. R., "Shuttle Entry Performance and Stability and Control Derivatives Extracted From Flight Measurement Data," AIAA Paper 82-1317, Aug. 1982.

[26]Ried, R. C, "A Flight Test Challenge: Aeroassist for Reusable, Space-Based Transportation," 9th Aerospace Testing Seminar, Los Angeles, CA, Oct. 1985.

[27]Park, C. and Yoon, S., "Calculation of Real-Gas Effects on Blunt-Body Trim Angles," AIAA Paper 89-0685, Jan. 1989.

[28]Crowder, R. S. and Moote, J. D., "Apollo Entry Aerodynamics," *Journal of Spacecraft and Rockets,* Vol. 6, No. 3, March 1969, pp. 302–307.

[29]Hillje, E. R. and Savage, R., "Status of Aerodynamics Characteristics of the Apollo Entry Configuration," AIAA Paper 68-1143, Dec. 1968.

[30]Nagamatzu, H. T., Geiger, R. E., and Sheer, R. E., Jr., "Hypersonic Shock Tunnel," *American Rocket Society Journal,* Vol. 29, No. 5, May 1959, pp. 332–340.

[31]Miller, C. G. III, "A Comparison of Measured and Predicted Sphere Shock Shapes in Hypersonic Flows with Density Ratios from 4 to 19," NASA TN D-8076, Dec. 1975.

[32]Lobb, R. K., "Experimental Measurements of Shock Detachment Distance on Spheres Fired in Air at Hypervelocities," *The High Temperature Aspects of Hypersonic Flow,* AGARDograph 68, edited by W. C. Nelson, Pergamon, Oxford, 1964, pp. 519–527.

[33]Spurk, J. H., "Experimental and Numerical Nonequilibrium Flow Studies," *AIAA Journal,* Vol. 8, 1970, pp. 1039–1045.

[34]Hornung, H. G., "Non-Equilibrium Dissociating Nitrogen Flow Over Spheres and Circular Cylinders," *Journal of Fluid Mechanics,* Vol. 53, Pt. 1, May 1972, pp. 149–176.

[35]Macrossan, M. N. and Stalker, R. J., "Afterbody Flow of a Dissociating Gas Downstream of a Blunt Nose," AIAA Paper 87-0407, Jan. 1987.

[36]Candler, G. V. and MacCormack, R. W., "The Computation of Hypersonic Flows in Chemical and Thermal Nonequilibrium," Third National Aero-Space Plane Technology Symposium, NASA Ames Research Center, Moffett Field, CA, 1987.

[37]Candler, G., "On the Computation of Shock Shapes in Nonequilibrium Hypersonic Flows," AIAA Paper 89-0312, Jan. 1989.

[38]Sharma, S. P., Huo, W. M., and Park, C., "The Rate Parameters for Coupled Vibration-Dissociation in a Generalized SSH Approximation" AIAA Paper 82-2714, June 1988.

[39]Oliver, R. E., "An Experimental Investigation of Flow About Simple Blunt Bodies at a Nominal Mach Number of 5.8," *Journal of the Aeronautical Sciences,* Vol. 23, No. 2, Feb. 1958, pp. 177–179.

[40]Desautel, D., "AOTV Bow Shock Location," AIAA Paper 85-1062, June 1985.

[41]Nagamatzu, H. T. and Shear, R. E., Jr., "Vibrational Relaxation and Recombination of Nitrogen and Air in Hypersonic Nozzle Flows," *AIAA Journal,* Vol. 3, No. 8, Aug. 1965, pp. 1386–1391.

[42]Nagamatzu, H. J., Workman, J. B., and Shear, R. E., Jr., "Oblique Shock Relations for Air at Mach 7.8 and 7200 R Stagnation Temperature," *American Rocket Society Journal,* Vol. 30, April 1960, pp. 619–623.

[43]Sharma, S. P. and Park, C., "Operating Characteristics of a 60 cm and a 10 cm Electric Arc-Driven Shock Tube," AIAA Paper 88-0142, Jan. 1988.

[44]Haasz, A. A. and Lever, J. H., "Schlieren Diagnostics of a Gas Target Neutron Generator," Univ. of Toronto, Inst. of Aerospace Studies, Toronto, Canada, UTIAS Rept. 242, Feb. 1980.

[45]Research Staff, National Physical Laboratory, *Schlieren Methods, Notes on Applied Science No. 31,* National Physical Lab., Teddington, England, UK, 1947.

[46]Killer, J. O., Saito, K., and Kishimoto, K., "An Experimental Investigation of a Pulse Combustor: Flow Visualization by Schlieren Photography," Sandia National Lab., Albuquerque, NM, SAND-84-8928 Nov. 1984.

[47]Goad, W. K. and Burner, A. W., "Holographic Flow Visualization at the Langley Expansion Tube," NASA TM-83116, June 1981.

[48]Hugenschmidt, M., Wey, J., and Baca, W., "Recent Development in High Speed Cinematographic and Interferometric Studies of High Power Laser Target Interactions," IEEE Publ. 81CH1712-9, 1981.

[49]Kittleson, J. K. and Yu, Y. H., "Transonic Rotor Flow-Measurement Technique Using Holographic Interferometry," *Proceedings of Ninth European Rotorcraft Forum,* 1983, pp. 3–10.

[50]Trolinger, I. D., Azazzy, M., Modarress, D., and Craig, J. E., "Laser Diagnostic Methods: A Summary," AIAA Paper 83-1683, July 1983.

[51]Veret, C., "Review of Optical Techniques with Respect to Aero-Engine Applications," Conference Proceedings for AGARD Lecture Series No. 90, Optical Measurement Methods with Laser for Research and Study of Aero-Engines, ONERA, Chatillon, France, Sept. 1977.

[52]Bachalo, W. D. and Houser, M. J., "Optical Interferometry in Fluid Dynamics Research," *Optical Engineering,* Vol. 24, No. 3, May–June 1985, pp. 455–461.

[53]Li, H. Y., Xu, C. Y., Shu, J., and Hu, J. M., "On the Capacity of Holographic Phase-Shift Interferometric Technique in the Visualization of Low Density Flows," *Acta Mechanics Sinica (China),* No. 1979, English Translation FTD, ID(RS)T-0705-81, National Technical Information Service, Springfield, VA, Sept. 1981.

[54]Carrigan B., "Holographic Flow Visualizastion: Citations From the Engineering Data Base 1970-April 1979," National Technical Information Service, Springfield, VA, Progress Rept. May 1979.

[55]Trolinger, J. D, "Aero-Optical Characterization of Aircraft Optical Turrets by Holograhy, Interferometry and Shadowgraph," NASA CP-2121, April 1980, pp. 127–152.

[56]Laufer, G. and McKenzie, R. L., "Temperature Measurements in Hypersonic Air Flows using Laser-Induced O_2 Fluorescence," AIAA Paper 88-4679-CP, 19.

[57]Lauafer, G., McKenize, R. L., and Huo, W. M., "Radiative Processes in Air Excited by an ArF Laser," *Optics Letters,* Vol. 13, Feb. 1988, pp. 99–101.

[58]Gross, K. P., McKenzie, R. L., and Logan, P., "Measurements of Temperature, Density, Pressure, and Their Fluctuations in Supersonic Turbulence Using Laser-Induced Fluorescence,"*Experiments in Fluids,* Vol. 5, No. 6, 1987, pp. 372–380.

[59]Eckbreth, A., *Laser Diagnostics for Combustion Temperature and Species,* edited by A. K. Gupta and D. G. Liley, Abacus, Cambridge, MA, 1988.

[60]Losev, S. A. and Generalov, N. A., "A Study of Excitation of Vibrations and Dissociation of Oxygen Molecules at High Temperatures," *Soviet Physics—Doklady,* Vol. 6, No. 12, June 1962, p. 1081.

[61]White, D. R. and Millikan, R. C., "Vibrational Relaxation of Oxygen," *Journal of Chemical Physics,* Vol. 39, No. 7, Oct. 1963, pp. 1803–1806.

[62]Millikan, R. C. and White, D. R., "Systematics of Vibrational Relaxation," *Journal of Chemical Physics,* Vol. 39, No. 12, Dec. 1963, pp. 3209–3213.

[63]Lee, J. H., "Electron-Impact Vibrational Excitation Rates in the Flowfield of Aeroassisted Orbital Transfer Vehicles," *Progress in Astronautics and Aeronautics: Thermophysical Aspects of Re-entry Flows,* Vol. 103, edited by J. N. Moss and C. D. Scott, AIAA, New York, 1986, pp. 197–224.

[64]Allen, R. A., "Nonequilibrium Shock Front Rotational, Vibrational and Electronic Temperature Measurements," AVCO Everett Research Lab., Everett, MA, Research Rept. 186, 1964.

[65]Dunn, M. G. and Lordi, J. A., "Measurement of $N_2^+ + e^-$ Dissociative Recombination in Expanding Nitrogen Flows," *AIAA Journal,* Vol. 8, No. 2, Feb. 1970, pp. 339–345.

[66]Guberman, S. L., "Theoretical Studies of Dissociative Recombination," *Progress in Astronautics and Aeronautics: Thermophysical Aspects of Re-entry Flows,* Vol. 103, edited by J. N. Moss and C. D. Scott, AIAA, New York, 1986, pp. 225–242.

[67]Park, C., "Measurement of Ionic Recombination Rate of Nitrogen," *AIAA Journal,* Vol. 6, Nov. 1968, pp. 2090–2094.

[68]Kang, S. W., Dunn, M. G., and Jones, W. L., "Theoretical and Measured Electron-Density Distributions for the RAM Vehicle at High Altitudes," AIAA Paper 72-689, June 1972.

[69]Wilson, J., "Ionization Rate of Air Behind Shock-Speed Shock Waves," *Physics of Fluids,* Vol. 9, No. 10, 1966, pp. 1913–1921.

[70]Candler, G. and Park, C., "The Computation of Radiation from Nonequilibrium Hypersonic Flows," AIAA Paper 88-2678, June 1988.

[71]Nagamatzu, H. T. and Shear, R. E., Jr., "Maganetohydrodynamic Results for Highly Dissociated and Ionized Air Plasma," *Physics of Fluids,* Vol. 4, No. 6, May 1961, pp. 1073–1084.

[72]Nagamatzu, H. T., Shear, R. E., Jr., and Weil, J. A., "Non-Linear Electrical Conductivity of Plasma for Magnetohydrodynamic Power Generations," American Rocket Society Paper 2632-62, Nov. 1962.

[73]Compton, D. L. and Cooper, D. M., "Duplication in a Shock Tube of Stagnation Region Conditions on a Jovian Atmospheric Entry Probe," *Recent Developments in Shock Tube Research,* edited by D. Bershader and W. Griffith, Stanford Univ. Press, Stanford, CA, 1973, pp. 318–329.

[74]Lofthus, A. and Krupenie, P. H., "The Spectrum of Molecular Nitrogen," *Journal of Physical and Chemical Reference Data,* Vol. 6, No. 1, Jan.–March 1977, pp. 113–307.

[75]Appleton, J. P. and Steinberg, M., "Vacuum-Ultraviolet Absorption of Shock-Heated Vibrationally Excited Nitrogen," *Journal of Chemical Physics,* Vol. 46, No. 4, Feb. 1967, pp. 1521–1529.

[76]Allen, F. A., Textoris, A., and Wilson, J., "Measurements of the Free-Bound and Free-Free Continua of Nitrogen, Oxygen and Air," *Journal of Quantitative Spectroscopy and Radiative Transfer,* Vol. 5, No. 1, Jan.–Feb. 1965, pp. 95–108.

[77]Churchill, D. R. and Meyerott, R. E., "Spectral Absorption in Heated Air," *Journal of Quantitative Spectroscopy and Radiative Transfer,* Vol. 5, No. 1, Jan.–Feb. 1965, pp. 65–86.

[78]Allen, R. A., "Air Radiation Tables: Spectral Distribution Functions for Molecular Band Systems," AVCO Everett Research Lab., Everett, MA, Research Rept. 236, April 1966.

[79]Pearse, R. W. B. and Gaydon, A. G., *The Identification of Molecular Spectra,* Chapman & Hall, London, 1963.

[80]Arnold, J. O., Cooper, D. M., Park, C., and Prakash, S. G., "Line-by-line Transport Calculations for Jupiter Entry Probes," *Progress in Astronautics and Aeronautics: Entry Heating and Thermal Protection,* Vol. 69, edited by W. B. Olstad, AIAA, New York, 1980, pp. 52–82.

[81]Park, C., "A Shock Tube Measurement of the $SiO(E^1\Sigma^+ - X^1\Sigma^+)$ Transition Moment," *Journal of Quantitative Spectroscopy and Radiative Transfer,* Vol. 20, No. 5, Nov. 1978, pp. 491–498.

[82]Wehrmeyer, J. A., Bowling, J. M., and Pitz, R. W., "Concentration, Temperature, and Density in a Hydrogen-Air Flame by Excimer-Induced Raman Scattering," Central States Meeting of the Combustion Institute, Indianapolis, IN, May 2–3, 1988.

[83]Hargis, P. J., Jr., "Trace Detection of Small Molecules by Pulsed-Ultraviolet (UV) Laser Raman Spectroscopy," *Laser Spectroscopy for Sensitive Detection,* Society of Photo-Optical Instrumentation Engineers, Bellingham, WA, Vol. 286, 1981.

[84]Tolles, W. M., Nibler, J. W., McDonald, J. R., and Harvey, A. B., "A Review of the Theory and Application of Coherent Anti-Stokes Spectroscopy (CARS)," *Applied Spectroscopy,* Vol. 31, No. 4, July–Aug. 1977, pp. 253–271.

[85]Eesley, G. L., *Coherent Raman Spectroscopy,* Pergamon, New York, 1981.

[86]Lapp, M. and Penney, C. M. (ed.), *Laser Raman Gas Diagnostics,* Plenum, New York, 1974.

[87]Haroche, S., Pebay-Peyroula, J. C., Hansch, T. W., and Harris, S. E., *Laser Spectroscopy, Proceedings of the Second International Conference on Laser Spectroscopy,* Springer-Verlag, New York, 1975.

[88]Hall, R. J., "CARS Spectra of Combustion Gases," *Combustion and Flame,* Vol. 35, No. 1, May 1979, pp. 47–60.

[89]Eckbreth, A. C., "CARS Thermometry in Practical Combustors," *Combustion and Flame,* Vol. 39, No. 2, Oct. 1980, pp. 133–148.

[90]Nitsch, W. and Kiefer, W., "High Resolution Pulsed CARS Spectroscopy of the Q-Branches of Some Simple Gases," *Optical Communications,* Vol. 23, No. 2, 1977, pp. 240–244.

[91]Tolles, W. M. and Turner, R. D., "A Comparative Analysis of the Analytical Capabilities of Coherent Anti-Stokes Raman Spectroscopy (CARS) Relative to Raman Scattering and Absorption Spectroscopy," *Applied Spectroscopy,* Vol. 31, No. 2, March–April 1977, pp. 96–103.

[92]Maier, M., Kaiser, W., and Giordmaine, J. A., "Backward Stimulated Raman Scattering," *Physical Review,* Vol. 177, No. 2, Jan. 1969, pp. 580–599.